GDCh

Research Articles

Angewandte
Chemie
International Edition
www.angewandte.org

CO₂ Reduction

Boosting Low-Temperature CO₂ Hydrogenation over Ni-based Catalysts by Tuning Strong Metal-Support Interactions

Runping Ye[+], Lixuan Ma[+], Xiaoling Hong[+], Tomas Ramirez Reina, Wenhao Luo,
Liqun Kang, Gang Feng, Rongbin Zhang, Maohong Fan,* Riguang Zhang,* and Jian Liu*

Abstract: Rational design of low-cost and efficient transition-metal catalysts for low-temperature CO_2 activation is significant and poses great challenges. Herein, a strategy via regulating the local electron density of active sites is developed to boost CO_2 methanation that normally requires $>350\,°C$ for commercial Ni catalysts. An optimal Ni/ZrO_2 catalyst affords an excellent low-temperature performance hitherto, with a CO_2 conversion of 84.0 %, CH_4 selectivity of 98.6 % even at 230 °C and GHSV of 12,000 $mL\,g^{-1}\,h^{-1}$ for 106 h, reflecting one of the best CO_2 methanation performance to date on Ni-based catalysts. Combined a series of in situ spectroscopic characterization studies reveal that re-constructing *monoclinic*-ZrO_2 supported Ni species with abundant oxygen vacancies can facilitate CO_2 activation, owing to the enhanced local electron density of Ni induced by the strong metal-support interactions. These findings might be of great aid for construction of robust catalysts with an enhanced performance for CO_2 emission abatement and beyond.

Introduction

Carbon dioxide (CO_2) utilization technology is under intensive development, given its key role in achieving carbon neutrality.[1] Under this global scenario and extensive applications of hydrogenation reactions,[2] CO_2 hydrogenation with green hydrogen from renewable energy is an effective approach to transforming CO_2 into chemicals and fuels.[3] Particularly, affording nearly quantitative selectivity towards methane and over 90 % equilibrium CO_2 conversion levels even under low temperatures ($<300\,°C$) and atmospheric pressure, CO_2 methanation brings a major superiority compared to other CO_2 hydrogenation processes.[4] In other

words, CO_2 methanation is deemed as an efficient strategy to convert a large amount of captured CO_2 into value-added synthetic natural gas, which could be further converted into other valuable products. Furthermore, CO_2 methanation could be applied to coal-to-gas, power-to-gas and CO_2 removal for spacecraft showcasing the versatility and broad range of applications of this catalytic process.[5]

As CO_2 methanation is an exothermic reaction, it is thermodynamically favored in the low temperatures range. However, the reaction kinetics counterbalance the exothermic nature imposing some energy barriers for reactants activation.[5a,6] Most of the previous studies report that the actual reaction temperatures for CO_2 methanation are

[*]   Prof. Dr. R. Ye,[+] Prof. Dr. G. Feng, Prof. Dr. R. Zhang
      Key Laboratory of Jiangxi Province for Environment and Energy
      Catalysis, Institute of Applied Chemistry, School of Chemistry and
      Chemical Engineering, Nanchang University
      Nanchang 330031 (P. R. China)

      X. Hong,[+] Prof. Dr. J. Liu
      State Key Laboratory of Catalysis, Dalian Institute of Chemical
      Physics, Chinese Academy of Sciences
      Dalian 116023, Liaoning (P. R. China)
      E-mail: jianliu@dicp.ac.cn

      L. Ma,[+] Prof. Dr. R. Zhang
      State Key Laboratory of Clean and Efficient Coal Utilization, College
      of Chemical Engineering and Technology, Taiyuan University of
      Technology
      Taiyuan 030024, Shanxi (P. R. China)
      E-mail: zhangriguang@tyut.edu.cn

      Prof. Dr. J. Liu
      DICP-Surrey Joint Centre for Future Materials, Department of
      Chemical and Process Engineering, and Advanced Technology
      Institute, University of Surrey
      Guilford, Surrey GU2 7XH (UK)

      Prof. Dr. M. Fan
      College of Engineering and Physical Sciences, and School of Energy
      Resources, University of Wyoming
      Laramie, WY 82071 (USA)
      E-mail: mfan@uwyo.edu

      Prof. Dr. W. Luo, Prof. Dr. J. Liu
      College of Chemistry and Chemical Engineering,
      Inner Mongolia University
      Hohhot 010021 (P. R. China)
      E-mail: jian.liu@imu.edu.cn

      Prof. Dr. T. R. Reina
      Department of Inorganic Chemistry and Material Sciences Institute
      of Seville, University of Seville-CSIC
      41092 Seville (Spain)

      Dr. L. Kang
      Max Planck Institute for Chemical Energy Conversion
      Stiftstraße 34–36, 45470 Mülheim an der Ruhr (Germany)

[+]   These authors contributed equally to this work.

higher than 350 °C.[7] Indeed, CO_2 is an inert gas with its σ bond and π bond activation demand relatively high temperatures. However, when a commercial application is envisaged, high temperatures may represent excessive energy consumption and impact the overall process operational costs. Moreover, upon raising the temperature the competitive reaction (reverse water gas shift, RWGS) begins to operate leading to higher selectivity towards CO as a by-product and also the catalyst deactivation due to active phase sintering.[8] Hence the bottleneck issue for CO_2 methanation is to develop a robust non-noble catalyst to activate CO_2 molecules and further hydrogenate them yielding methane at low reaction temperatures.

Generally, noble metal-based catalysts present efficient low-temperature performance of CO_2 methanation, but they are not practical options for large-scale applications due to their elevated costs.[9] Alternatively, Ni-based catalysts present high performance for CO_2 methanation at a generally high reaction temperature (>350 °C).[10] To improve their activity, many strategies have been developed from different perspectives, such as enhancing Ni loading (ω_{Ni}),[11] changing the Ni particle size (d_{Ni}),[12] doping of the second metal,[13] improving the strong metal-support interactions (SMSI),[14] and optimizing the catalyst structure.[15] Among them, tuning the properties of supports, such as their crystal phases, specific surface areas, surface acidity or basicity, pore structures, support's particle sizes and oxygen vacancies could obviously affect CO_2 methanation performance.[16] We have previously demonstrated that Ni/*monoclinic*-ZrO_2 catalyst could afford a superior activity for CO_2 hydrogenation compared to Ni/*cubic*-ZrO_2 catalyst.[16a] Similarly, a series of Co/CeO_2-ZrO_2 catalysts with different particle sizes of CeO_2-ZrO_2 support could lead to various CO_2 methanation performance owing to the size-dependent metal-support interactions and oxygen vacancies.[16b] The particle size of CeO_2-ZrO_2 with ≈20 nm supported Co nanoparticles exhibited better performance due to higher Co dispersion and facile formation of oxygen vacancies. Moreover, the properties of supports could further tune the SMSI and then influence catalytic performance.[17] For example, the effect of SMSI on the methane selectivity and catalytic activity during CO_2 methanation have been demonstrated over Ni/Ru/Co-based catalysts.[9b,16b,18] However, the optimal reaction temperatures over these reported catalysts for CO_2 methanation were still higher than 300 °C.

In this contribution, three Ni-based catalysts (Ni/SiAlZr) with different supports (SiO_2, Al_2O_3, ZrO_2) and strong metal-support interactions were prepared by sol-gel method for CO_2 methanation. Also, a reference Ni/ZrO_2-IM sample was prepared by impregnation method (IM). As a result, the Ni/ZrO_2 catalyst exhibited an extraordinary low-temperature property with a CO_2 conversion of 84.0 % and methane selectivity of 98.6 % even at 230 °C. The effect of local electron density on Ni active sites and the exceptional performance of Ni/ZrO_2 has been investigated by a series of experimental characterizations.

Results and Discussion

Three Ni-based catalysts with SiO_2, Al_2O_3 and ZrO_2 as supports have been synthesized and evaluated in fix-bed reactor. CO_2 hydrogenation over a series of Ni/SiAlZr catalysts was firstly performed under different reaction temperatures. As shown in Figure 1a, the Ni/ZrO_2 presents the highest CO_2 conversion ($Conv._{CO2}$) of 91.9 % at 240 °C, while the Ni/SiO_2, Ni/ZrO_2-IM and commercial Ni samples exhibit much lower $Conv._{CO2}$ under identical reaction conditions. The CH_4 selectivity ($Sel._{CH4}$) over Ni/SiAlZr catalysts is almost 100 %, except that Ni/SiO_2 presents an obvious CO product under low reaction temperatures. It has been reported that the CO selectivity over Ni/SiO_2 catalysts would be affected by many factors, such as reaction conditions, preparation method, Ni loading, and silica structure (Table S1).[19] Furthermore, the $Conv._{CO2}$ over Ni/ZrO_2 could reach up to 50 % at only 210 °C while that for Ni/Al_2O_3, Ni/SiO_2 and commercial Ni catalysts is 234, 273 and 268 °C, respectively (Figure 1b and Figure S1). Therefore, the activity order over the Ni/SiAlZr catalysts is Ni/ZrO_2 > Ni/Al_2O_3 ≫ Ni/SiO_2 — Commercial Ni catalyst > Ni/ZrO_2-IM. The effect of Ni loading on Ni/ZrO_2 has been further investigated. It indicates that the $Conv._{CO2}$ increases significantly, while the $Sel._{CH4}$ is almost the same in spite of the increase of Ni loading (Figure S2). Thus, the Ni-based catalysts with high Ni loading show better CO_2 activation activity and the 40 % Ni/ZrO_2 catalyst exhibits the best catalytic performance here.

As the Ni/ZrO_2 in this work displays exceptionally high activity for CO_2 methanation under low reaction temperatures, the comparison of Ni/ZrO_2 and some reported representative Ni-based catalysts are illustrated in Figure 1c and Table S2. The Ni/ZrO_2 reported here exhibits high $Conv._{CO2}$ and space-time yield (STY, 311.2 $mmol_{CH4} g_{cat}^{-1} h^{-1}$) of methane, which is much higher (3–115 times) than those over the previously reported Ni/ZrO_2 catalysts (2.7–89.9 $mmol_{CH4} g_{cat}^{-1} h^{-1}$) under similar reaction conditions. For the other typical Ni-based catalysts listed in Table S2, the Ni/ZrO_2 presented herein still shows a much lower reaction temperature and higher STY_{CH4}. Therefore, to the best of our knowledge, our engineered catalyst takes the edge over the state-of-the-art materials in this field.

Beyond the advanced catalytic activity showcased by the Ni/ZrO_2, its stability tests were performed at 230 °C and gas hour space velocity (GHSV) of 12,000 $mL g^{-1} h^{-1}$ (Figure 1d). The $Conv._{CO2}$ and $Sel._{CH4}$ were able to maintain above 80 % and 98 % even after a time on steam of 106 h, respectively. Furthermore, the Ni/ZrO_2 was stable under more severe reaction conditions (220 °C, 24,000 $mL g^{-1} h^{-1}$). However, the $Conv._{CO2}$ could still maintain at around 45 % without obvious deactivation (Figure 1d). In addition, we repeated the stability test of Ni/ZrO_2 catalyst under low temperatures of 200, 230 300 °C and high GHSV of 48,000 $mL g^{-1} h^{-1}$, and it still presented prominent stability (Figure S3). Based on various characterization results of the fresh and spent Ni/ZrO_2 (Figure S4 and Figure S5), no apparent issues of metal sintering and coke formation can
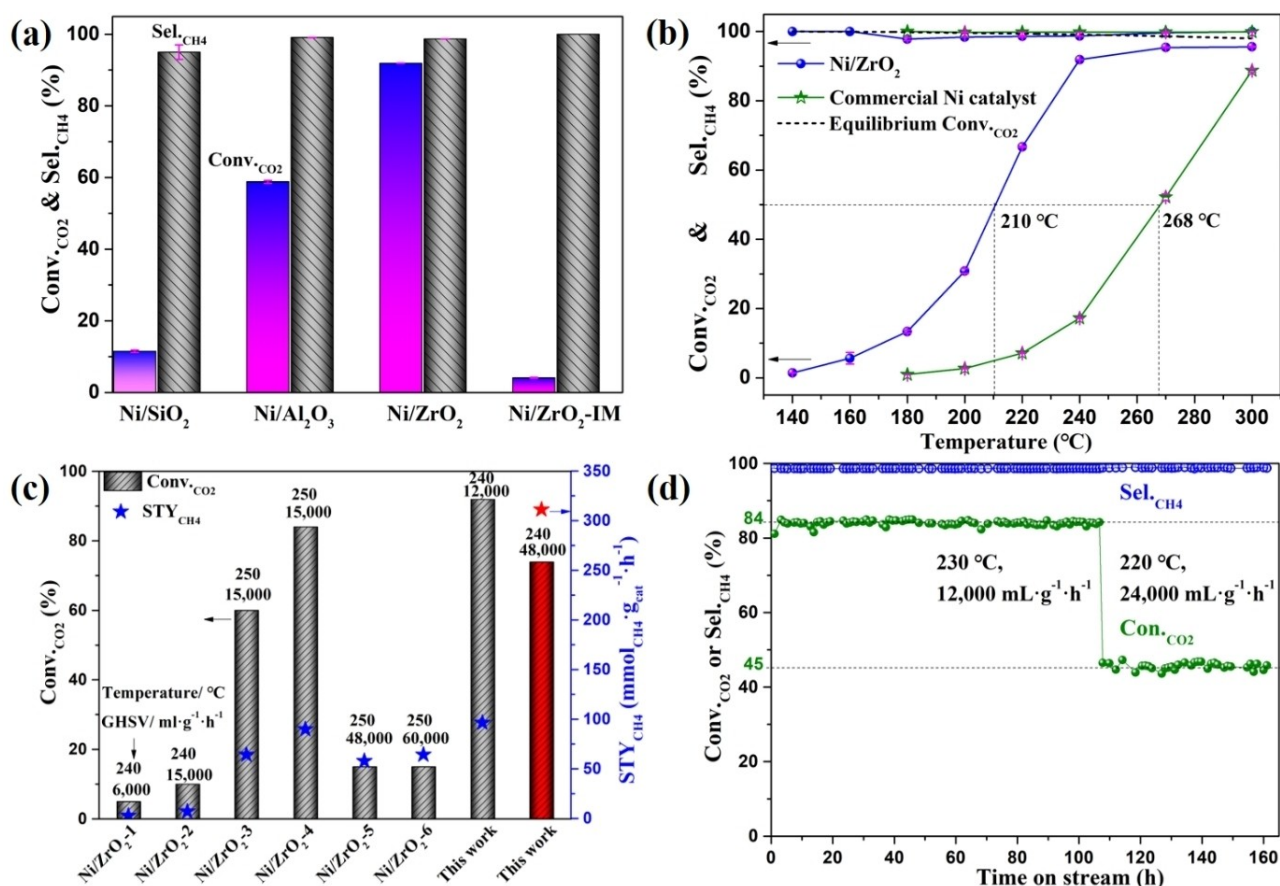
Figure 1. CO_2 hydrogenation performance over Ni/SiAlZr catalysts. (a) Catalytic performance at 240 °C and GHSV of 12,000 mL g^{-1} h^{-1}. (b) Conv.$_{CO2}$ and Sel.$_{CH4}$ over Ni/ZrO$_2$ and commercial Ni catalysts under different reaction temperatures. (c) The Ni/ZrO$_2$ compared to other reported Ni/ZrO$_2$ catalysts at 240–250 °C. More detailed information on the reported Ni/ZrO$_2$ catalysts is listed in Table S2. (d) The long-term stability of Ni/ZrO$_2$ catalyst at 220–230 °C and GHSV of 12,000–24,000 mL g^{-1} h^{-1}.

be indicated upon catalysis, confirming the superior stability of Ni/ZrO$_2$ catalyst.

We further test their structural and textual properties based on the remarkable activity of Ni/ZrO$_2$ catalysts. The actual Ni loading over Ni/SiO$_2$ was only 32.91 wt %, which was much lower than that ($\approx$40 wt %) over other Ni/SiAlZr catalysts (Table 1). The reason was probably that there was not enough hydroxyl on the surface of silicon oxide to anchor the high concentration of nickel species, which resulted in some nickel species being evaporated during the process of evaporating the water to form gel. Would the lower Ni loading on Ni/SiO$_2$ lead to much lower catalytic performance than Ni/ZrO$_2$? The 30 % Ni/ZrO$_2$ exhibited a much higher Conv.$_{CO2}$ (64.9 %) than that over Ni/SiO$_2$

(11.5 %) at 240 °C. In our previous work, a Ni/SiO$_2$ catalyst with 44.4 wt % content of Ni still only presented a low Conv.$_{CO2}$ of $\approx$30 % at 250 °C.[20] Liu et al. also deeply investigated why Ni/CeO$_2$ with 10.0 wt % of Ni was more active than Ni/SiO$_2$ with 25.9 wt % of Ni for CO_2 methanation.[21] The reason was attributed to the tiny Ni particle size for large H$_2$ uptake capacity and more oxygen vacancies for CO_2 activation on the Ni/CeO$_2$. Therefore, we can exclude the influence of Ni content on the catalytic results and the support species would significantly affect the catalytic performance.

Figure S6 and Table 1 display the N$_2$ physisorption results of Ni/SiAlZr catalysts. The shape of the isotherm on Ni/SiO$_2$ is much different from the others, but its specific

Table 1: The physicochemical properties of Ni/SiAlZr catalysts.

Catalysts	ω_{Ni} [wt.%]	S_{BET} [m^2/g]	D_p [nm]	V_p [cm^3/g]	D_{Ni} [%]	SA_{Ni} [m^2/g]	d_{Ni} [nm]	TOF [$\times 10^{-3}$ s^{-1}]
Ni/SiO$_2$	32.91	156.3	11.9	0.45	6.45	14.13	14.7	1.6
Ni/Al$_2$O$_3$	41.18	216.0	3.0	0.14	6.08	16.68	11.0	8.7
Ni/ZrO$_2$	42.83	84.3	3.2	0.06	3.15	8.98	14.6	39.6
Ni/ZrO$_2$-IM	40.03	20.8	7.5	0.04	1.17	3.12	39.3	1.7

surface area (S_{BET}) and average pore diameter (D_p) as well as pore volume (V_p) were much larger than those over Ni/ ZrO_2. The Ni/Al_2O_3 exhibits the largest S_{BET} of 216.0 m²/g, while the Ni/ZrO_2-IM displays only 20.8 m²/g. It suggests that some nickel species were covered in the pores of Ni/ ZrO_2-IM, and the S_{BET} would not affect the catalytic performance.

H₂ pulse chemisorption was carried out to determine the Ni dispersion (D_{Ni}) and Ni surfaces area (SA_{Ni}). As a result, the Ni/ZrO_2 shows a D_{Ni} of 3.15 %, which is lower than Ni/ SiO_2 and Ni/Al_2O_3 catalysts while higher than Ni/ZrO_2-IM catalyst (Table 1). The particle size of Ni nanoparticles on Ni/ZrO_2 (14.6 nm) is similar to that on the Ni/SiO_2 and Ni/ Al_2O_3, but much smaller than that on the Ni/ZrO_2-IM (39.3 nm). Based on the above data, turnover frequency (TOF) values were further employed to compare their catalytic performance at 200 °C (Table 1). It shows that the TOF value over Ni/ZrO_2 is much higher than the others.

The crystalline phases of calcined and reduced samples were measured by XRD. The small diffraction peaks of Ni metal could be observed over the samples prepared by the sol-gel method, while the Ni/ZrO_2-IM presents sharp diffraction peaks of NiO or Ni, indicating that much larger nickel species were formed on the Ni/ZrO_2-IM. A weak amorphous silica or aluminum oxide peak could also be observed over the Ni/SiO_2 and Ni/Al_2O_3 samples (Figure 2a). Interestingly, the ZrO_2 support over the calcined Ni/ ZrO_2 sample displays diffraction peaks of cubic zirconia (c-ZrO_2, PDF#03-0640, Figure S7), while the reduced and especially the used Ni/ZrO_2 samples present some obvious

peaks of monoclinic zirconia (m-ZrO_2, PDF#05-0543, Figure 2a). It suggests that the Ni/ZrO_2 could be reconstructed by changing the crystal form of ZrO_2 during hydrogen activation and CO_2 methanation. In our previous work,[16a] the Ni/m-ZrO_2 possessed high activity for this reaction than the Ni/c-ZrO_2 due to their diverse local electron density of Ni.

To further analyze the nickel species and the reduction behavior of Ni/SiAlZr catalysts, H₂-TPR profiles were obtained and shown in Figure 2b. The reduction peak of Ni/ SiO_2 is obviously smaller than that of the others, which is consistent with the ICP result that shows lower Ni loading. Furthermore, the large asymmetric reduction peaks from 100 to 600 °C could be fitted by a Gaussian-type function into three small reduction peaks (Figure S8). The first one (α) centered at around 200 °C is attributed to the reduction of NiO weakly interacting with oxide supports and active adsorbed oxygen species. The second reduction peak (β) centered at around 300 °C can be assigned to the hydrogen consumption on the reduction of nickel species in the interfacial structure of Ni-O-Si (Al or Zr). The last one (γ) reduction peak centered at around 425 °C mainly corresponds to highly dispersed NiO with strong metal-support interactions.[22] The H₂-TPR suggests that the nickel species over Ni/ZrO_2 could be easier to be reduced than the other two samples, demonstrating that the metal interacts strongly with support on the Ni/SiO_2 and Ni/Al_2O_3 catalysts. In addition, the CO_2-TPD tests were operated to determine the surface basicity of Ni/SiAlZr catalysts. Figure 2c shows that the peaks belonging to the weak basic sites at 50–150 °C are
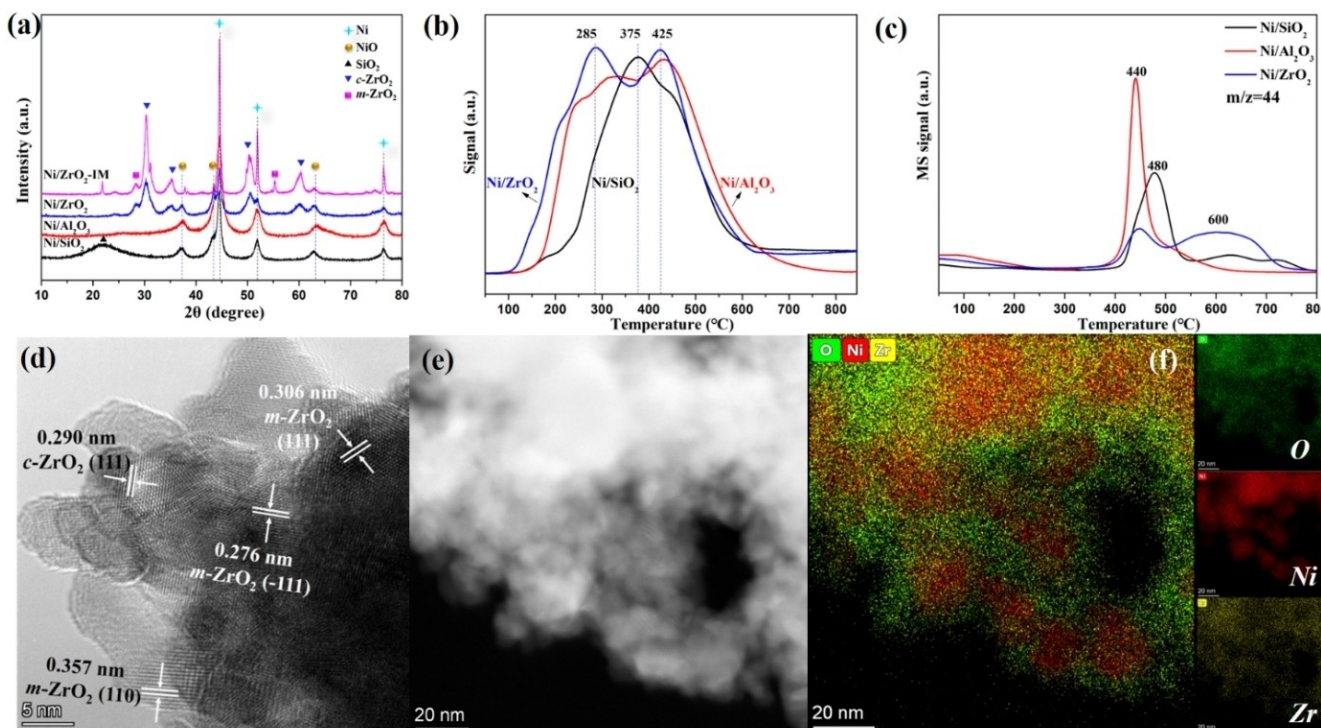

Figure 2. The physicochemical properties of Ni/SiAlZr catalysts. (a) XRD patterns of reduced Ni/SiAlZr catalysts. (b) H₂-TPR profiles of Ni/SiAlZr catalysts. (c) CO_2-TPD profiles of Ni/SiAlZr catalysts. (d-f) HAADF and HRTEM images with corresponding elemental mapping of Ni/ZrO_2 catalyst.

very weak, while most of the desorption peaks are attributed to the medium-strength (150–500 °C) and strong basic sites (500–750 °C). The Ni/ZrO$_2$ possesses the strongest CO$_2$ desorption peaks while the Ni/Al$_2$O$_3$ is the opposite, indicating that the Ni/SiO$_2$ and Ni/Al$_2$O$_3$ mainly exhibit medium-strength basic sites while those over the Ni/ZrO$_2$ are the strong basic sites. From previous literature reports,[22a] we know that medium-strength basic sites are mainly associated with acid-base metal oxides and Ni-O^{2-} pairs, while the strong basic sites can be caused by surface coordinatively unsaturated Lewis basic sites of O^{2-} species. The peaks around 500–750 °C can be attributed to the CO$_2$ adsorption on the strong basic sites and surface oxygen vacancies.[23] The Ni/ZrO$_2$ sample has more surface oxygen vacancies and thus presents a larger peak around 500–750 °C. More importantly, the CO$_2$ at the high-temperature desorption peak would be converted to the formation of HCO$_3^-$ or CO$_3^{2-}$, leading to the strong basicity.[24] As the CO$_2$-TPD test did not flow hydrogen, the HCO$_3^-$ or CO$_3^{2-}$ could not be further converted to methane. During CO$_2$ hydrogenation, the HCO$_3^-$ or CO$_3^{2-}$ could be converted to other intermediates and the final methane product. In addition, it was reported that the CO$_2$ methanation performance was correlated with the strength of the basicity of the catalyst.[24] The Ni/ZrO$_2$ catalyst with stronger basic sites presented better catalytic properties. Therefore, the metal species are various among the Ni/SiAlZr catalysts, with the Ni/ZrO$_2$ exhibiting more reduced nickel species and strong basic sites while metal interacts the strongest with support on the Ni/Al$_2$O$_3$ with medium-strength basic sites.

Figure 2d–f and Figures S9–S13 present the electron microscope images of Ni/SiAlZr catalysts. The SEM images show that the Ni/ZrO$_2$ exhibits abundant large pores (Figure S9), probably produced through citric acid decomposition. These large pores are beneficial for gas flow and mass transfer. TEM images were further obtained to observe the Ni nanoparticles (NPs) and other elemental distribution. Figure 2e–f and Figures S10–S11 display that Ni NPs are highly dispersed over the SiO$_2$, Al$_2$O$_3$, and ZrO$_2$ supports. The mean particle size over Ni/SiO$_2$ is slightly higher than that over Ni/Al$_2$O$_3$ (Figure S10). For the Ni/Al$_2$O$_3$, the TEM and corresponding EDS mapping images show that the Ni nanoparticles are encapsulated by a thin Al$_2$O$_3$ layer (Figure S11), which results in slightly larger Ni particle sizes determined by H$_2$ pulse chemisorption than the XRD results (11.0 nm vs. 16.7 nm). It was reported that the palladium or Ni nanoparticles were decorated with a thin layer of an aluminate phase or nickel aluminate layer, which indicates that the SMSI exhibits in the Al$_2$O$_3$-based catalysts.[25]

Different catalyst structures could be inferred from TEM results with a further comparison between Ni/ZrO$_2$ and Ni/ZrO$_2$-IM by the HRTEM and HAADF-STEM images (Figure 2d–f and Figures S12–S13). For the HRTEM images of Ni/ZrO$_2$, crystal planes belonging to the *m*-ZrO$_2$ and *c*-ZrO$_2$ could be obviously observed while that for the Ni or NiO are difficult to observe (Figure 2d). The *d* values of the distances between adjacent lattice fringes in Ni/ZrO$_2$ catalsyt are slightly shorter than those in the bulk *m*-ZrO$_2$ (Figure 2d). The elemental mapping further shows that Ni

metals are separated and embraced by the Zr and O elements on the Ni/ZrO$_2$ (Figure 2f and Figure S12). The situation for the Ni/ZrO$_2$-IM is opposite, which presents many obvious crystal planes belonging to Ni or NiO (Figure S13). Therefore, the TEM results indicate that some Ni NPs are uniformly incorporated into the lattice of ZrO$_2$ and surrounded by the Zr and O elements on the Ni/ZrO$_2$. The literatures have already reported that Ni nanoparticles could be incorporated into mesoporous amorphous ZrO$_2$ matrix and ZrO$_2$-CeO$_2$ supports.[26] The extent of SMSI over Ni/SiAlZr catalysts is different and the SMSI is obvious on the Ni/ZrO$_2$ and weak on the Ni/Al$_2$O$_3$ while SMSI is lacking on the Ni/SiO$_2$ catalyst.

The X-ray photoelectron spectroscopy (XPS) was also employed to investigate the chemical state and surface compositions of the Ni/SiAlZr catalysts. Firstly, the *quasi in situ* XPS spectroscopy on the Ni/ZrO$_2$ catalyst under different processes was also investigated and shown in Figure 3 and Table S3. For the Ni 2p spectra, it shows that most of the nickel species over the calcined Ni/ZrO$_2$ sample are Ni^{2+} species at $\approx$855.3 eV and corresponding satellite peaks at $\approx$860.6 eV. After reduction by hydrogen, the ratio of Ni^0/(Ni^0+Ni^{2+}) increased from 9.6% to 44.1% and then increased up to 55.2–58.3% during CO$_2$ methanation. It proves that most of the nickel species are Ni^0 species during CO$_2$ hydrogenation reaction. The binding energy (BE) of Ni^0 2p$_{3/2}$ on Ni/ZrO$_2$ is $\approx$852.5 eV, which is much lower than the others and reported bulk Ni^0, demonstrating that the electronic density of Ni was increased by the SMSI.[27] Therefore, some of Ni atoms (Ni$^{\delta-}$) were negatively charged by electron transfer from ZrO$_2$ support, which is consistent with the chemical state and surface compositions of Ni 2p in the Ni-Bi catalyst.[28] The defective ZrO$_2$ support with abundant oxygen vacancies can trap negative electrons at its center and then transfer to Ni at the interface. In addition, the negatively charged metals from the supports due to metal-support interactions have also been observed over Ru/TiO$_2$,[29] Cu/ZnO,[30] and Pd/Ga$_2$O$_3$ catalysts for other hydrogenation reactions.[31] Furthermore, the O 1s spectra can be divided into three peaks. Namely, the former two peaks (O$_\alpha$ and O$_\beta$) can be attributed to the surface adsorbed oxygen species (O$^-$ or O$_2^{2-}$, O$_2^-$), and the last peak (O$_\gamma$) is belonged to lattice oxygen (O^{2-}).[32] The surface adsorbed oxygen species may come from the surface hydroxyl groups, transformation of the surface adsorbed O$_2$ molecules, defect oxide, and CO$_3^{2-}$.[33] The surface lattice oxygen ratio over the calcined Ni/ZrO$_2$ sample (54.9%) was slightly decreased to around 50.2% while the ratio of Zr^{3+}/(Zr^{3+}+Zr^{4+}) increased from 18.2% to around 22.8% after reduction and CO$_2$ methanation. For the Zr 3d spectra, the Zr^{4+} species have two strong peaks at $\approx$181.5 eV and $\approx$184.0 eV while the Zr^{3+} species from partial reduction of Zr^{4+} have two weak peaks at $\approx$180.5 eV and $\approx$182.5 eV.[22b,34] The BE of Zr 3d$_{5/2}$ on Ni/ZrO$_2$ catalyst (180.5–181.5 eV) was much lower than the value of Zr^{4+} ions in ZrO$_2$ (183.5 eV), which was because that surface Zr centers are coordinatively unsaturated and have lower oxidation states due to the dangling bond, indicating that Zr^{4+} on the surface has been partly reduced to Zr^{3+}.[33b] The ratio of Zr^{3+}/(Zr^{3+}+Zr^{4+})
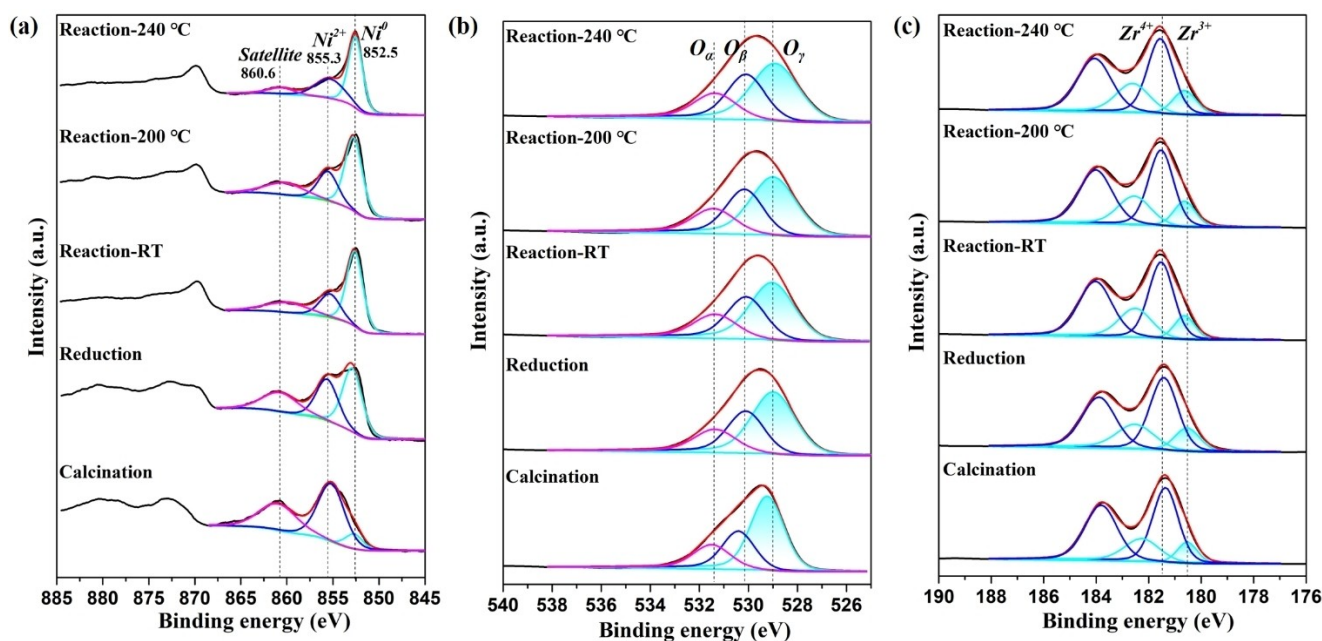
Figure 3. *Quasi* in situ XPS spectra of (a) Ni 2p, (b) O 1s, and (c) Zr 3d over Ni/ZrO$_2$ catalysts after calcination, *quasi* in situ reduction by H$_2$, *quasi* in situ reaction under the atmosphere of CO$_2$ and H$_2$ at room temperature (RT), 200 °C and 240 °C.

suggests the relative concentrations of the oxygen vacancies. It indicates that more oxygen vacancies are produced after reduction and the oxygen vacancies are stable because the O 1s and Zr 3d peaks are stable during reaction. Thus, oxygen vacancies on the Ni/ZrO$_2$ catalyst are involved in CO$_2$ methanation reaction. The oxygen vacancies in the Ni/ZrO$_2$ sample was also demonstrated by the pyridine-infrared spectroscopy (Py-IR). The peaks at 1445 cm^{-1} is attributed to the Lewis acid sites, which are from coordinatively unsaturated Zr^{3+} and Zr^{4+} as well as the oxygen vacancies.[35] The specific amount of Lewis acid sites can be quantified by the area of the peak at 1445 cm^{-1} with the calculation formula at the end of Table S4. The Ni/ZrO$_2$ exhibits a slightly lower amount of Lewis acid sites than pure ZrO$_2$ support but a higher amount of Lewis acid sites than Ni/ZrO$_2$-IM sample, suggesting that a moderate amount of oxygen vacancies are present over Ni/ZrO$_2$ sample (Figure S14).

For the control samples, the XPS results are illustrated in Figure S15 and Table S5. Firstly, the surface Ni atom ratio (24.3 %) on the Ni/ZrO$_2$-IM is obviously higher than the others (6.7–9.9 %), indicating that more nickel species sintering on Ni/ZrO$_2$-IM catalyst prepared by impregnation method while the other catalysts would have more Ni species encapsulated by the supports. Secondly, the Ni 2p and O 1s on the Ni/ZrO$_2$-IM is much different from the others. Namely, the Ni/ZrO$_2$-IM has more obvious peaks of Ni^0 species and lattice oxygen. The main nickel species from ex situ XPS test over the control samples are Ni^{2+}, which is probably from the quick re-oxidation of active Ni^0 to Ni^{2+} or unreduced Ni^{2+} as proved by the above H$_2$-TPR. It is obvious that Ni/ZrO$_2$-IM exhibits more lattice oxygen (52.7 %) from crystalline ZrO$_2$ than Ni/SiO$_2$ and Ni/Al$_2$O$_3$.

The latter two catalysts exhibit 9.3–11.0 % of lattice oxygen that probably originates from the crystalline NiO. Although the Ni/SiO$_2$ and Ni/Al$_2$O$_3$ possess more surface adsorbed oxygen species for CO$_2$ methanation, their catalytic performances are still lower than Ni/ZrO$_2$.

In addition, X-ray absorption spectra (XAS) were performed to account for the difference in the Ni-O-Zr coordination structure between the main sample and the control samples, and the results are shown in Figure 4, Figures S16–S18 and Table S6. For the Ni K-edge X-ray absorption near-edge structure (XANES) and extended X-ray absorption fine structure (EXAFS) spectra, the trends in edge positions and the whiteline intensities are all in line with the actual compositions of the Ni catalysts obtained from the EXAFS analysis. The first shell Ni-O and Ni-Ni paths are characteristic for Ni oxides and Ni metal. The second shell Ni-Ni path is taken to complete the NiO structure. Based on the XRD characterization results, it is reasonable to believe the majority of Ni species are present in the form of Ni metal and Ni oxides, which is consistent with the XPS results. From the fitting results, we could see the bond lengths are in good agreement with the Ni-O and Ni-Ni distances in bulk Ni metal and NiO phase (Table S6). The only noticeable difference is that the two Ni-Ni distances are slightly longer than those in Ni metal and NiO, suggesting the expanded lattice distances due to the formation of mixed phases. The Debye–Waller factor is significantly bigger than those in typical Ni foil and NiO, which means the coordination structure of the Ni sites is strongly disordered, corresponding well with the broad FWHM of the XRD diffraction peaks. Furthermore, it is worth mentioning that in addition to the shorter Ni-Ni scattering path, the longer Ni-Ni scattering path could be
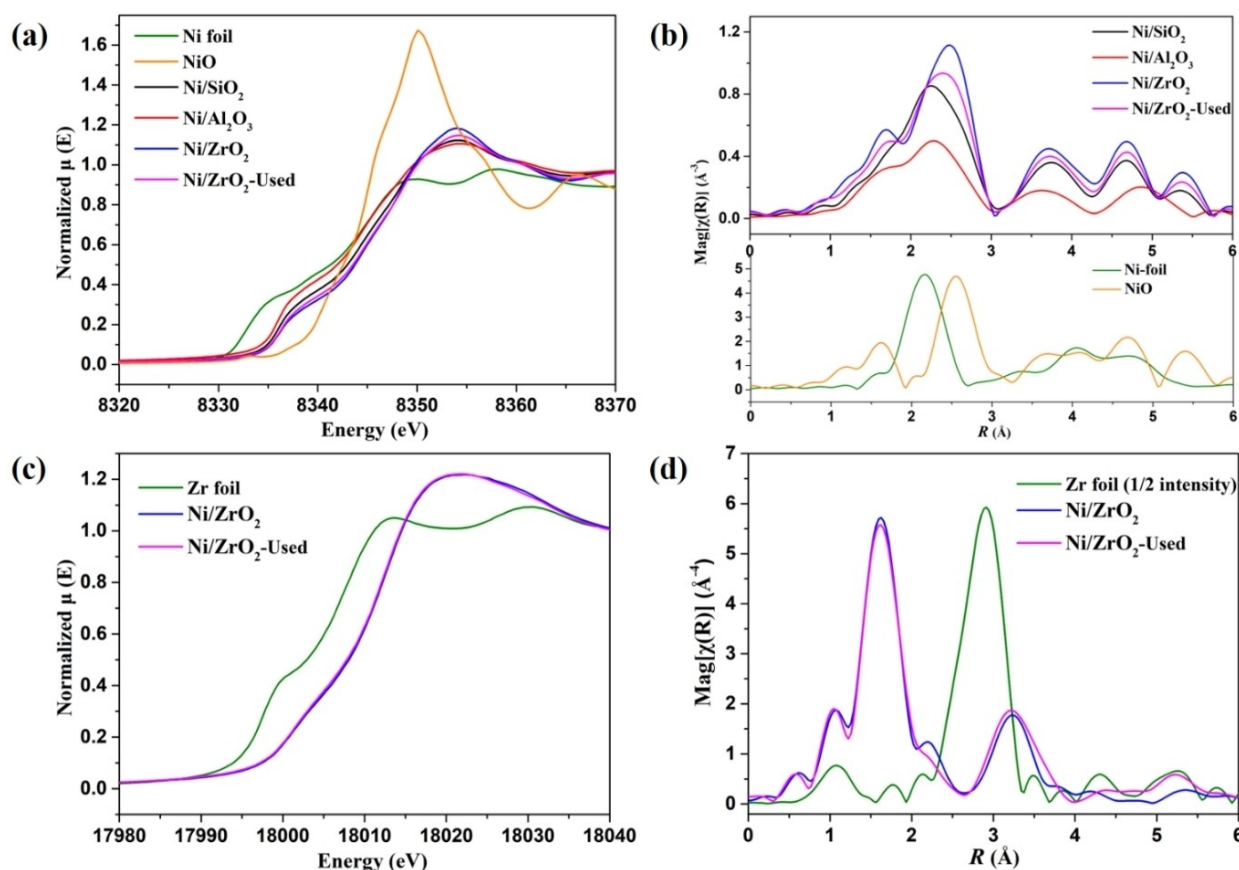
Figure 4. Ni K-edge and Zr K-edge XAS spectra of Ni/SiAlZr catalysts. (a, c) XANES spectra (normalized) and (b, d) k^2 or k^3-weighted R-space EXAFS spectra.

replaced by a Ni-Zr scattering. With Zr as a slightly heavier back scatter, the mathematical EXAFS fitting could still get converged, showing similar coordination numbers and Debye–Waller factors. But the calculated Ni-Zr distance is around 2.85 Å, which is significantly shorter than typical Zr-Zr distances in Zr oxides. Therefore, most of the Ni species are still loaded on the surface of ZrO_2. For the Zr K-edge XANES and EXAFS (Figure 4 and Figure S18), the Zr-O and Zr-Zr distances are in good agreement with the average Zr-O and Zr-Zr distances in the ZrO_2 structure. Actually, they were slightly shorter than the ideal bond lengths. Similarly, the huge Debye–Waller factors for the Zr-Zr paths suggest that the ZrO_2 structure is highly disordered. The coordination number (C.N.) for the Zr-O path is less than typical cubic ZrO_2 (C.N.=8) and monoclinic ZrO_2 (C.N.=7). This indicates the ZrO_2 supports exhibit surface coordinatively unsaturated Zr centers with highly disordered structure.

To explore the reaction mechanism, a series of experimental measurements were operated. Firstly, the temperature programmed surface reaction (TPSR) of CO_2 methanation was carried out to investigate CO_2 activation and possible reaction products under different reaction temperatures. The detailed test procedures are shown in the Supporting Information. As depicted in Figure S19, all the peak areas of both the thermal conductivity detector (TCD)

signal and mass spectrometry (MS) signal on Ni/ZrO$_2$-IM are lower than those appeared on Ni/ZrO$_2$, indicating that the surface of Ni/ZrO$_2$ is better for CO_2 adsorption and activation than that over the Ni/ZrO$_2$-IM. We could obtain the following important information from Figure 5a and Figure S19c. CO_2 could be detected only at a temperature lower than $\approx 150\,°C$, indicating that the left CO_2 at the higher temperature was consumed by hydrogen. Also, when the temperature was higher than $100\,°C$, the peak of CH_4 at m/z of 16 on Ni/ZrO$_2$ began to increase and reached two vertexes at 180 and $626\,°C$, respectively. This result suggests that CO_2 could be activated to form methane at the extremely low reaction temperature, which is consistent with the activity test and the temperature is also much lower than that reported over the mesoporous Ni/CeO$_2$-ZrO$_2$ catalyst.[36] The large peak of CH_4 formation at around $626\,°C$ indicates that the surface of Ni/ZrO$_2$ exhibits strong basic sites for CO_2 adsorption as also demonstrated by CO_2-TPD. In addition, a large peak of CO formation at around $626\,°C$ on Ni/ZrO$_2$ is mainly due to the RWGS reaction that is favourable occurred at high reaction temperatures.

Furthermore, in situ DRIFT spectra were collected to identify the surface species and speculate on the possible reaction mechanism, as depicted in Figure 5b and Figures S20–S23. As the Conv.$_{CO2}$ is still very high at $240\,°C$ for Ni/ZrO$_2$, its in situ CO_2 methanation was operated at $210\,°C$
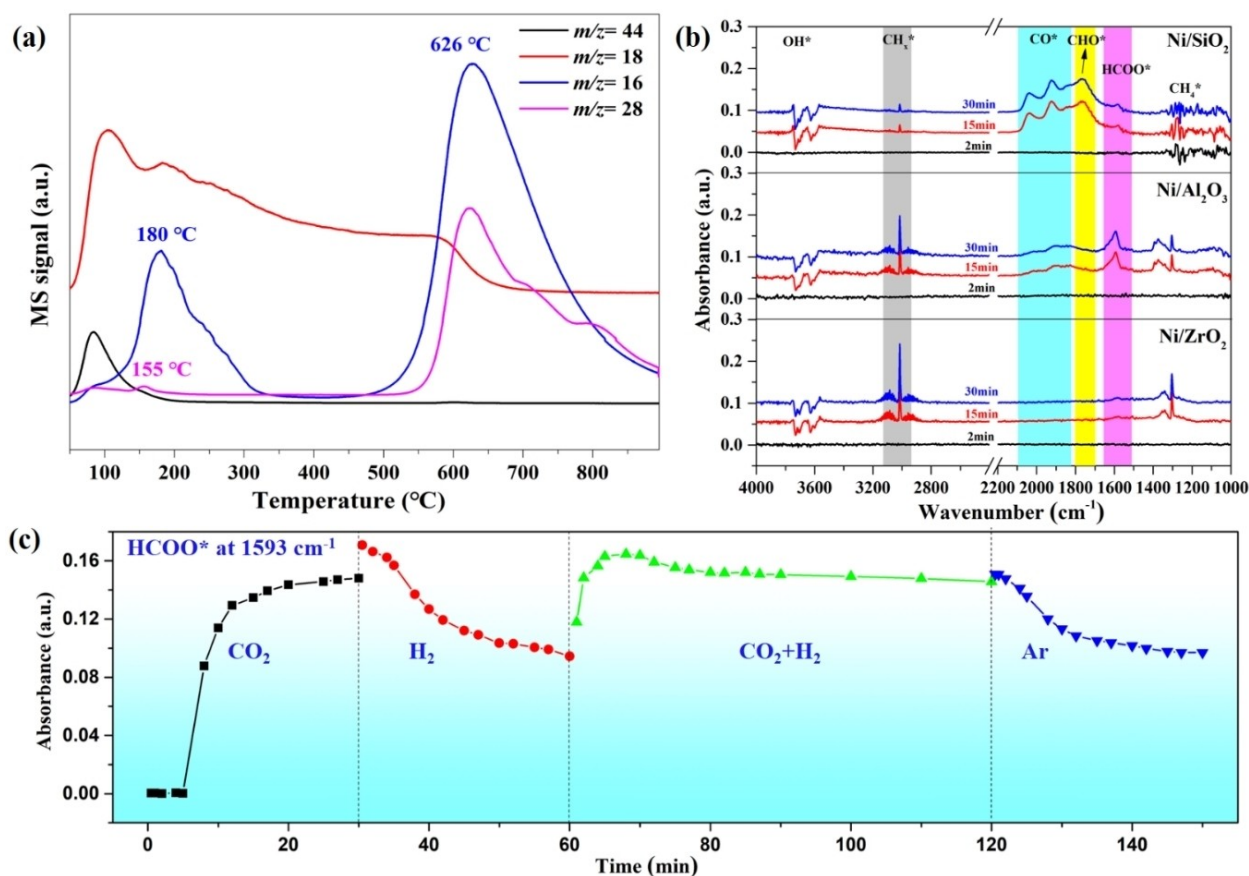
Figure 5. The results of the potential reaction mechanism. (a) The TPSR profiles of Ni/ZrO$_2$, Note: CO$_2$: $m/z=44$, H$_2$O: $m/z=18$, CH$_4$: $m/z=16$, CO: $m/z=28$. (b) The results of in situ DRIFTS tests on CO$_2$ hydrogenation over Ni/SiAlZr catalysts. The reaction temperature for Ni/SiO$_2$ and Ni/Al$_2$O$_3$ was 240 °C while for Ni/ZrO$_2$ was 210 °C. (c) Transient in situ DRIFTS experiments on Ni/ZrO$_2$ catalyst collected at 210 °C when the reaction atmospheres were switched from CO$_2$ to H$_2$, CO$_2$+H$_2$, and Ar. The peak intensity of HCOO* species at 1593 cm^{-1} as a function of time.

while the other two samples were operated at 240 °C to observe the possible reaction intermediates. As a result, the key surface species over Ni/SiAlZr catalysts are much different. For the Ni/SiO$_2$, we can observe the strong peaks of CO* linearly adsorbed on Ni sites (2040, 1920 cm^{-1}) and bridged CO* on active sites (1852 cm^{-1}) as well as CHO* (1760 cm^{-1}). However, the formate peak at 1585 cm^{-1} is very weak. For the Ni/Al$_2$O$_3$, the intensities of CO* and CHO* peaks decrease much while the intensity of formate increases considerably. Furthermore, the CO* and CHO* peaks could not be observed for Ni/ZrO$_2$, which only presents the formate peak at 1593 cm^{-1} as the key intermediate. The CO* mainly originated from dissociative adsorption of CO$_2$ and decomposition of formate species. Thus, the reaction mechanism changes from a dissociative mechanism to an associative mechanism when the support is switched from SiO$_2$ to ZrO$_2$. The other important surface species such as CH$_x$, methane, carbonates, and surface hydroxyl groups could also be detected, as shown in Figure 5b and Figures S20–S23.

To further verify the reaction mechanism of Ni/ZrO$_2$, the in situ DRIFTS spectra on the reference samples were also obtained (Figure S22). The Ni/ZrO$_2$-IM only presents some hydroxyl groups and a weak formate peak, without

showing the peaks of CO* and even the carbonates and methane. Similarly, only some peaks of hydroxyl groups and carbonates could be found on the pure ZrO$_2$ support. It suggests that the ZrO$_2$ support is significant for CO$_2$ adsorption and activation, while the Ni metal is beneficial for hydrogen activation and further hydrogenation of intermediates. Therefore, the Ni/ZrO$_2$ possesses suitable exposed Ni metals and Ni-O-Zr as well as abundant oxygen vacancies that are active for CO$_2$ methanation through the direct formate hydrogenation pathway, which was also demonstrated by the transient in situ DRIFTS experiments. As shown in Figure S23 and Figure 5c, the Ni/ZrO$_2$ catalyst was firstly exposed to pure CO$_2$ then the system was switched to other reaction atmospheres, resulting in considerable change of the surface species. Different types of hydroxyl groups at around 3733–3590 cm^{-1} belonged to bicarbonates species that appeared and increased after the introduction of CO$_2$ gas. The bicarbonates were generated from CO$_2$ adsorption on OH$^-$ groups of ZrO$_2$ support.[37] The observation of obvious hydroxyl groups at around 3750–3500 cm^{-1} was also reported in Ni/Al$_2$O$_3$,[37] Ru/CeCrO$_x$,[38] and LaNiO$_3$/CeO$_2$ catalysts during in situ DRIFTS test of CO$_2$ methanation.[39] Some other carbonates (1637, 1273, 1250, 1050 cm^{-1}) and formate (1593, 1369 cm^{-1})

peaks have also presented in Figure S23a.[40] It indicates that these surface species could not be further converted and there was no peak belonging to *CO and *CH4. The formate formation was because that chemisorbed CO_2 reacted with hydrogen available on the catalyst surface (Figure S23a), which was consistent with the in situ DRIFTS results over Ru/CeO_2 catalyst for the formate formation under CO_2/He and H_2/He atmospheres.[41] López-Rodríguez et al. also observed formate peak under CO_2/He atmosphere and then decreased under H_2/He atmosphere.[41] After 30 mins, the gas was switched to hydrogen. The peaks of hydroxyl groups disappeared quickly, and the other peaks of carbonates and formate also became much weaker (Figure S23a). Upon switching the reaction atmosphere from hydrogen to $CO_2 + H_2$ (1:4 v/v), new peaks can be observed at 3015 and 1301 cm^{-1}, which are attributed to *CH$_x$ and methane (Figure S23b).[42] With time increased, the intensities of *CH$_x$ and methane peaks increased while the intensities of peaks attributed to hydroxyl groups, carbonates and formate decreased, which suggests that these are the important reaction intermediates. In particular, the intensity of formate increased quickly and then decreased slightly. Finally, the gas flow was switched to Ar, and most of the peaks disappeared while a small formate peak at 1593 cm^{-1} still could be observed (Figure S23b), indicating that it could be stably adsorbed. This was maybe because the reaction time was not enough and the reaction temperature was low. The strong basic sites and surface oxygen vacancies over Ni/ZrO_2 could adsorb these reaction intermediates. The variation tendency of formate intensity as a function of time is illustrated in Figure 5c. It clearly shows that the formate could be produced and increased in the $CO_2/CO_2 + H_2$ atmospheres due to CO_2 reaction with surface OH groups.[22b] During the whole test procedure, the peaks attributed to CO* could not be observed. In addition, the ion chromatography results show that the amount of formate was 3.1 mg/L at 230 °C and increased to 15.7 mg/L at 200 °C, suggesting that formate is an important intermediate. Therefore, the HCOO* path instead of CO* is the main reaction path for CO_2 methanation on the Ni/ZrO_2 catalyst, which was also consistent with the literature reports.[22b,43]

Conclusion

In summary, extraordinary low-temperature CO_2-methanation catalysts have been designed and synthesized in this work. Characterizations like TEM, XPS, and Py-IR showcase regulation of the SMSI and oxygen vacancies, which further affect the local electron density of active sites. Furthermore, the chemisorption and activation of CO_2 and H_2 dissociation would be affected, and thus influence the catalytic results through different reaction pathways from a dissociative mechanism over Ni/SiO_2 to an associative mechanism over Ni/ZrO_2. Experimental results further prove that the Ni/ZrO_2 catalyst with a re-constructed structure of more *monoclinic* ZrO_2 species displays outstanding catalytic behaviour outperforming the benchmark Ni-based catalysts and even superior to a wide range of

noble metal-based catalysts reported so far. Indeed, methane formation on Ni/ZrO_2 is kinetically and thermodynamically way more advantageous compared to a Ni/SiO_2 catalyst. This work opens new research avenues to design robust catalysts for CO_2 hydrogenation based on the regulation of SMSI and then the local electron density of reaction active sites. Therefore, it is crucial to tune SMSI by engineering the support properties and metal loading methods toward boosting low-temperature CO_2 hydrogenation performance.

Conflict of Interest

The authors declare no conflict of interest.

Data Availability Statement

The data that support the findings of this study are available from the corresponding author upon reasonable request.

[1] a) C. Hepburn, E. Adlen, J. Beddington, E. A. Carter, S. Fuss, N. Mac Dowell, J. C. Minx, P. Smith, C. K. Williams, *Nature* **2019**, *575*, 87–97; b) J. Ding, Q. Tang, Y. Fu, Y. Zhang, J. Hu, T. Li, Q. Zhong, M. Fan, H. H. Kung, *J. Am. Chem. Soc.* **2022**, *144*, 9576–9585.

[2] a) X. Ren, M. Guo, H. Li, C. Li, L. Yu, J. Liu, Q. Yang, *Angew. Chem. Int. Ed.* **2019**, *58*, 14483–14488; b) C. Dong, Q. Yu, R. P. Ye, P. Su, J. Liu, G. H. Wang, *Angew. Chem. Int. Ed.* **2020**, *59*, 18374–18379.

[3] a) R. P. Ye, J. Ding, W. Gong, M. D. Argyle, Q. Zhong, Y. Wang, C. K. Russell, Z. Xu, A. G. Russell, Q. Li, M. Fan, Y. G. Yao, *Nat. Commun.* **2019**, *10*, 5698; b) J. Wang, G. Li, Z. Li, C. Tang, Z. Feng, H. An, H. Liu, T. Liu, C. Li, *Sci. Adv.* **2017**, *3*,

Angew. Chem. Int. Ed. **2024**, *63*, e202317669 (9 of 11)

© 2023 The Authors. Angewandte Chemie International Edition published by Wiley-VCH GmbH

e1701290; c) S. Kattel, P. J. Ramírez, J. G. Chen, J. A. Rodriguez, P. Liu, *Science* **2017**, *355*, 1296–1299; d) X. Wang, R. Ye, M. S. Duyar, C. A. H. Price, H. Tian, Y. Chen, N. Ta, H. Liu, J. Liu, *Nano Res.* **2023**, *16*, 5601–5609; e) D. Xu, Y. Wang, M. Ding, X. Hong, G. Liu, S. C. E. Tsang, *Chem* **2021**, *7*, 849–881.

[4] J. J. Gao, Y. L. Wang, Y. Ping, D. C. Hu, G. W. Xu, G. W. Gu, F. B. Su, *RSC Adv.* **2012**, *2*, 2358–2368.

[5] a) C. Vogt, M. Monai, G. J. Kramer, B. M. Weckhuysen, *Nat. Catal.* **2019**, *2*, 188–197; b) S. Chen, A. M. Abdel-Mageed, M. Dyballa, M. Parlinska-Wojtan, J. Bansmann, S. Pollastri, L. Olivi, G. Aquilanti, R. J. Behm, *Angew. Chem. Int. Ed.* **2020**, *59*, 22763–22770.

[6] F. Wang, S. He, H. Chen, B. Wang, L. Zheng, M. Wei, D. G. Evans, X. Duan, *J. Am. Chem. Soc.* **2016**, *138*, 6298–6305.

[7] Y. Du, C. Qin, C. Xu, D. Xu, J. Bai, G. Ma, M. Ding, *Chem. Eng. J.* **2021**, *418*, 129402.

[8] a) L. Yang, L. Pastor-Pérez, S. Gu, A. Sepúlveda-Escribano, T. R. Reina, *Appl. Catal. B* **2018**, *232*, 464–471; b) Q. Zhang, L. Pastor-Pérez, W. Jin, S. Gu, T. R. Reina, *Appl. Catal. B* **2019**, *244*, 889–898.

[9] a) J. Cored, A. Garcia-Ortiz, S. Iborra, M. J. Climent, L. Liu, C. H. Chuang, T. S. Chan, C. Escudero, P. Concepcion, A. Corma, *J. Am. Chem. Soc.* **2019**, *141*, 19304–19311; b) H. Xin, L. Lin, R. Li, D. Li, T. Song, R. Mu, Q. Fu, X. Bao, *J. Am. Chem. Soc.* **2022**, *144*, 4874–4882.

[10] R. P. Ye, L. Liao, T. R. Reina, J. Liu, D. Chevella, Y. Jin, M. Fan, J. Liu, *Fuel* **2021**, *285*, 119151.

[11] M. A. A. Aziz, A. A. Jalil, S. Triwahyono, M. W. A. Saad, *Chem. Eng. J.* **2015**, *260*, 757–764.

[12] C. Vogt, E. Groeneveld, G. Kamsma, M. Nachtegaal, L. Lu, C. J. Kiely, P. H. Berben, F. Meirer, B. M. Weckhuysen, *Nat. Catal.* **2018**, *1*, 127–134.

[13] D. De Masi, J. M. Asensio, P. F. Fazzini, L. M. Lacroix, B. Chaudret, *Angew. Chem. Int. Ed.* **2020**, *59*, 6187–6191.

[14] J. Li, Y. Lin, X. Pan, D. Miao, D. Ding, Y. Cui, J. Dong, X. Bao, *ACS Catal.* **2019**, *9*, 6342–6348.

[15] a) X. L. Yan, W. Sun, L. M. Fan, P. N. Duchesne, W. Wang, C. Kubel, D. Wang, S. G. H. Kumar, Y. F. Li, A. Tavasoli, T. E. Wood, D. L. H. Hung, L. L. Wan, L. Wang, R. Song, J. L. Guo, I. Gourevich, A. A. Jelle, J. J. Lu, R. F. Li, B. D. Hatton, G. A. Ozin, *Nat. Commun.* **2019**, *10*, 2608; b) A. Parastaev, V. Muravev, E. H. Osta, T. F. Kimpel, J. F. M. Simons, A. J. F. van Hoof, E. Uslamin, L. Zhang, J. J. C. Struijs, D. B. Burueva, E. V. Pokochueva, K. V. Kovtunov, I. V. Koptyug, I. J. Villar-Garcia, C. Escudero, T. Altantzis, P. Liu, A. Béché, S. Bals, N. Kosinov, E. J. M. Hensen, *Nat. Catal.* **2022**, *5*, 1051–1060.

[16] a) L. Ma, R. Ye, Y. Huang, T. R. Reina, X. Wang, C. Li, X. L. Zhang, M. Fan, R. Zhang, J. Liu, *Chem. Eng. J.* **2022**, *446*, 137031; b) A. Parastaev, V. Muravev, E. Huertas Osta, A. J. F. van Hoof, T. F. Kimpel, N. Kosinov, E. J. M. Hensen, *Nat. Catal.* **2020**, *3*, 526–533.

[17] P. Wu, S. Tan, J. Moon, Z. Yan, V. Fung, N. Li, S. Z. Yang, Y. Cheng, C. W. Abney, Z. Wu, A. Savara, A. M. Momen, D. E. Jiang, D. Su, H. Li, W. Zhu, S. Dai, H. Zhu, *Nat. Commun.* **2020**, *11*, 3042.

[18] T. Pu, J. Chen, W. Tu, J. Xu, Y.-F. Han, I. E. Wachs, M. Zhu, *J. Catal.* **2022**, *413*, 821–828.

[19] a) A. Cherevotan, B. Ray, S. R. Churipard, K. Kaur, U. K. Gautam, C. P. Vinod, S. C. Peter, *Appl. Catal. B* **2022**, *317*, 121692; b) H. C. Wu, Y. C. Chang, J. H. Wu, J. H. Lin, I. K. Lin, C. S. Chen, *Catal. Sci. Technol.* **2015**, *5*, 4154–4163; c) K. Wang, Y. Men, S. Liu, J. Wang, Y. Li, Y. Tang, Z. Li, W. An, X. Pan, L. Li, *Fuel* **2021**, *304*, 121388; d) Y. Xu, Y. Wu, J. Li, S. Wei, X. Gao, P. Wang, *Int. J. Hydrogen Energy* **2021**, *46*, 20919–20929; e) Y. R. Dias, O. W. Perez-Lopez, *J. Environ. Chem. Eng.* **2021**, *9*, 104629.

[20] L. Liao, L. Chen, R. P. Ye, X. Tang, J. Liu, *Chem. Asian J.* **2021**, *16*, 678–689.

[21] J. Liu, X. Wu, Y. Chen, Y. Zhang, T. Zhang, H. Ai, Q. Liu, *Int. J. Hydrogen Energy* **2022**, *47*, 6089–6096.

[22] a) P. Hongmanorom, J. Ashok, P. Chirawatkul, S. Kawi, *Appl. Catal. B* **2021**, *297*, 120454; b) X. Jia, X. Zhang, N. Rui, X. Hu, C. J. Liu, *Appl. Catal. B* **2019**, *244*, 159–169.

[23] Y. Yang, Z. Chai, X. Qin, Z. Zhang, A. Muhetaer, C. Wang, H. Huang, C. Yang, D. Ma, Q. Li, D. Xu, *Angew. Chem. Int. Ed.* **2022**, *61*, e202200567.

[24] M. Cai, J. Wen, W. Chu, X. Cheng, Z. Li, *J. Nat. Gas Chem.* **2011**, *20*, 318–324.

[25] a) A. S. Ivanova, E. M. Slavinskaya, R. V. Gulyaev, V. I. Zaikovskii, O. A. Stonkus, I. G. Danilova, L. M. Plyasova, I. A. Polukhina, A. I. Boronin, *Appl. Catal. B* **2010**, *97*, 57–71; b) J. L. Ewbank, L. Kovarik, F. Z. Diallo, C. Sievers, *Appl. Catal. A* **2015**, *494*, 57–67.

[26] a) H. S. Roh, K.-W. Jun, W. S. Dong, S. E. Park, Y. S. Baek, *Catal. Lett.* **2001**, *74*, 31–36; b) J. A. Montoya, E. Romero-Pascual, C. Gimon, P. Del Angel, A. Monzón, *Catal. Today* **2000**, *63*, 71–85; c) J. Ashok, M. L. Ang, S. Kawi, *Catal. Today* **2017**, *281*, 304–311; d) X. Zhang, Q. Zhang, N. Tsubaki, Y. Tan, Y. Han, *Fuel* **2015**, *147*, 243–252.

[27] J. Ni, W. Leng, J. Mao, J. Wang, J. Lin, D. Jiang, X. Li, *Appl. Catal. B* **2019**, *253*, 170–178.

[28] L. Chen, Z. Song, S. Zhang, C. K. Chang, Y. C. Chuang, X. Peng, C. Dun, J. J. Urban, J. Guo, J. L. Chen, D. Prendergast, M. Salmeron, G. A. Somorjai, J. Su, *Science* **2023**, *381*, 857–861.

[29] A. M. Abdel-Mageed, D. Widmann, S. E. Olesen, I. Chorkendorff, J. Biskupek, R. J. Behm, *ACS Catal.* **2015**, *5*, 6753–6763.

[30] F. Liao, Y. Huang, J. Ge, W. Zheng, K. Tedsree, P. Collier, X. Hong, S. C. Tsang, *Angew. Chem. Int. Ed.* **2011**, *50*, 2162–2165.

[31] X. Zhou, J. Qu, F. Xu, J. Hu, J. S. Foord, Z. Zeng, X. Hong, S. C. Tsang, *Chem. Commun.* **2013**, *49*, 1747–1749.

[32] a) K. Liu, X. Xu, J. Xu, X. Fang, L. Liu, X. Wang, *J. CO2 Util.* **2020**, *38*, 113–124; b) H. Liu, L. Liu, L. Wei, B. Chu, G. Qin, Z. Tong, L. Dong, B. Li, *Fuel* **2020**, *272*, 117738.

[33] a) J. Xu, Y. Zhang, X. Xu, X. Fang, R. Xi, Y. Liu, R. Zheng, X. Wang, *ACS Catal.* **2019**, *9*, 4030–4045; b) M. Zhang, J. Zhang, Y. Wu, J. Pan, Q. Zhang, Y. Tan, Y. Han, *Appl. Catal. B* **2019**, *244*, 427–437.

[34] a) M. Romero-Sáez, A. B. Dongil, N. Benito, R. Espinoza-González, N. Escalona, F. Gracia, *Appl. Catal. B* **2018**, *237*, 817–825; b) M. A. Rahman, S. Rout, J. P. Thomas, D. McGillivray, K. T. Leung, *J. Am. Chem. Soc.* **2016**, *138*, 11896–11906.

[35] a) V. Nichele, M. Signoretto, F. Pinna, F. Menegazzo, I. Rossetti, G. Cruciani, G. Cerrato, A. Di Michele, *Appl. Catal. B* **2014**, *150–151*, 12–20; b) R. Ding, Y. Wu, Y. Chen, H. Chen, J. Wang, Y. Shi, M. Yang, *Catal. Sci. Technol.* **2016**, *6*, 2065–2076.

[36] L. Xu, X. Wen, M. Chen, C. Lv, Y. Cui, X. Wu, C.-e. Wu, B. Yang, Z. Miao, X. Hu, *Fuel* **2020**, *282*, 118813.

[37] A. Quindimil, J. A. Onrubia-Calvo, A. Davó-Quiñonero, A. Bermejo-López, E. Bailón-García, B. Pereda-Ayo, D. Lozano-Castelló, J. A. González-Marcos, A. Bueno-López, J. R. González-Velasco, *J. CO2 Util.* **2022**, *57*, 101888.

[38] X. Xu, L. Liu, Y. Tong, X. Fang, J. Xu, D. Jiang, X. Wang, *ACS Catal.* **2021**, *11*, 5762–5775.

[39] J. A. Onrubia-Calvo, S. López-Rodríguez, I. J. Villar-García, V. Pérez-Dieste, A. Bueno-López, J. R. González-Velasco, *Appl. Catal. B* **2024**, *342*, 123367.

[40] a) Y. Guo, S. Mei, K. Yuan, D. J. Wang, H. C. Liu, C. H. Yan, Y. W. Zhang, *ACS Catal.* **2018**, *8*, 6203–6215; b) Y. Chai, B. Qin, B. Li, W. Dai, G. Wu, N. Guan, L. Li, *Natl. Sci. Rev.* **2023**, *10*, nwad043.

[41] S. López-Rodríguez, A. Davó-Quiñonero, E. Bailón-García, D. Lozano-Castelló, A. Bueno-López, *J. Mol. Catal.* **2021**, *515*, 111911.

[42] R. P. Ye, Q. Li, W. G. Gong, T. Wang, J. J. Razink, L. Lin, Y. Y. Qin, Z. Zhou, H. Adidharma, J. Tang, A. G. Russell, M. Fan, Y. G. Yao, *Appl. Catal. B* **2020**, *268*, 118474.

[43] L. Hu, A. Urakawa, *J. CO2 Util.* **2018**, *25*, 323–329.